

Photoanode modification of dye-sensitized solar cells with Ag/AgBr/TiO₂ nanocomposite for enhanced cell efficiency

I.H.K. Madigasekara^a, H.C.S. Perera^{b,*}, J.M.K.W. Kumari^{a,c}, G.R.K. Senadeera^{c,d}, M.A.K. L. Dissanayake^c

^a Postgraduate Institute of Science, University of Peradeniya, Peradeniya, Sri Lanka

^b Department of Physics, University of Peradeniya, Peradeniya, Sri Lanka

^c National Institute of Fundamental Studies, Kandy, Sri Lanka

^d Department of Physics, The Open University of Sri Lanka, Nawala, Nugegoda, Sri Lanka

ARTICLE INFO

Keywords:

Dye sensitized solar cells
Ag/AgBr nanocomposite
Surface plasmon resonance
Photosensitive semiconductor
Efficiency enhancement

ABSTRACT

Ag/AgBr compounds are well renowned visible light photosensitizers with inherent stability issues due to decomposition of the halide to metallic silver under illumination. However, when loaded onto a wide bandgap semiconductor with a more positive conduction band (i.e. TiO₂) than that of AgBr, they become much more stable after some initial decomposition. Stabilization occurs due to transfer of extra electrons that could combine with interstitial Ag⁺ to form Ag⁰ clusters to the wide bandgap semiconductor. Even though Ag/AgBr/TiO₂ nanocomposites are widely used in photocatalytic applications, their use in dye-sensitized solar cells have not been reported to date. In this work we incorporated an Ag/AgBr/TiO₂ nanocomposite which was successfully synthesized via a one-pot synthesis procedure to DSC active material and obtained an enhanced power conversion efficiency (PCE) of 8.46%. The increase in PCE is an impressive 31% compared to the PCE of 6.45% of the reference cell made with P25 TiO₂. The enhanced efficiency can be attributed to the synergistic effects rendered by both AgBr and metallic Ag. AgBr is highly efficient in generating electron – hole pairs under ≈ 470 nm visible light. Plasmonically enhanced effects introduced by Ag nanoparticles further improve the charge generation and separation both in the dye and AgBr. These cumulative effects combined with the stability maintained by the TiO₂ matrix of the DSC active material results in an efficiently performing DSC due to the incorporation of Ag/AgBr/TiO₂ nanocomposite into the photoanode.

1. Introduction

Dye-sensitized solar cells (DSCs) being a developing PV technology is intensively explored at present due to their lightweight, simple, flexible design which enables versatility in mounting platforms, easy green processing methods used, transparency, ability to function even in diffused daylight and overall cost efficiency (Andualem and Demiss, 2019; Gong et al., 2017; Mariotti et al., 2020; Mehmood et al., 2014; Sharma et al., 2018). However, DSCs still lag behind in terms of efficiency, durability and stability thus hampering their commercial applications. To overcome these drawbacks, much attention is focused on improving the photoanode. Among other materials (Mehmood et al., 2014; Sharma et al., 2018), a nanocrystalline mesoporous TiO₂ matrix is more commonly used as the wide bandgap semiconductor in the photoanode due to its ideal morphological and optical properties,

abundance, stability and non-toxicity (O'Regan and Grätzel, 1991).

Herein, we explored the possibility of incorporating Ag/AgBr/TiO₂ nanocomposite, a well-known highly efficient photocatalytic material in the DSC photoanode for improved cell performance. Silver bromide or AgBr is a photosensitive semiconductor (band gap 2.6 eV), and have been identified as such as early as in 1839 (Becquerel, 1839). However, their application in photovoltaics has not been pursued further due to the unstable nature of the compound. Under constant illumination AgBr absorbs photons generating electron-hole pairs where the photoelectrons reduce interstitial Ag⁺ ions to Ag⁰, and Ag⁰ nucleate to form metallic Ag nanoparticles (Ag NPs) (Zhang et al., 2018), which is an unavoidable phenomenon. However, it has been identified that these Ag⁰ clusters sensitize AgBr to a wider range of visible photons due to a self-sensitization mechanism explained by Calzaferri et al. (2001) ultimately sensitizing the AgX compound to respond to a broader spectral

* Corresponding author.

E-mail address: chanip@sci.pdn.ac.lk (H.C.S. Perera).

<https://doi.org/10.1016/j.solener.2021.10.015>

Received 14 May 2021; Received in revised form 16 September 2021; Accepted 6 October 2021

0038-092X/© 2021 International Solar Energy Society. Published by Elsevier Ltd. All rights reserved.

range in the visible spectrum. The formed Ag nanoclusters have also been identified to introduce localized electric field enhancement encouraging more electron-hole generation and fast charge separation due to Localized Surface Plasmon Resonance (LSPR) effects (Jiang et al., 2012; Wang et al., 2009, 2012b), thus, contributing to enhanced photoresponses and photocatalytic activity.

Kakuta et al. (1999) reported on obtaining much more stable systems by anchoring Ag/AgBr to wide bandgap semiconductor supports (i.e. SiO₂). Hu et al. (2006) also showed stability enhancement due to the presence of TiO₂ attached to Ag/AgBr nanoparticles. A detailed proposition to explain these effects has been brought forward by X. Wang et al. (2012). Ag NPs exhibit LSPR effect in the visible and near-infrared regions, and AgBr can be excited by light with wavelengths (λ) \approx 470 nm. Hence, both LSPR of Ag nanoparticles and excitation of AgBr could occur in the Ag/AgBr/TiO₂ nanocomposite system under visible light irradiation thereby improving the photoanode's photoresponse. These studies confirm the synergy of the Ag/AgBr/TiO₂ composite in enhancing photocatalytic activity whilst maintaining stability through vectorial charge transfer mechanisms; (1) AgBr – Ag – TiO₂ for photoelectrons generated in AgBr, (2) Ag – TiO₂ for plasmon induced electrons in Ag NPs, and (3) Ag – AgBr for plasmon induced holes of Ag NPs. Most photogenerated electrons are thought to be injected in to the TiO₂ conduction band (CB) and the photo induced holes, to the AgBr valance band (VB). Such separation of charges is understood to be faster when Ag/AgBr nanocomposites are firmly anchored to the TiO₂ matrix. Here, TiO₂ appears to be acting as a reservoir for electrons, significantly minimizing the number of electrons available in AgBr that can further reduce the interstitial Ag⁺, resulting in a stable photoanode system. Further proof of this mechanism is given in many reports based on similar systems (Gan et al., 2019; Hou et al., 2011; Rawal et al., 2013; D. Wang et al., 2012; Yang et al., 2016; Zhang et al., 2017).

Ag plasmonic NPs have been extensively utilized for PCE enhancement in DSCs (Kumari et al., 2019; Li et al., 2011; Pal et al., 2017). However, application of AgBr photosensitive nanoparticles/composite synergistic approach in dye-sensitized solar cells was yet to be explored. We observed that the energy landscape of the composite is favorable as a photosensitizer of a DSC and in fact may complement the cell action. As the component dedicated to photon absorption and charge generation, the photosensitizer of a DSC is of utmost importance. Among other sensitizers, ruthenium (II) polypyridyl complexes such as N719, N3, and black dye, show the highest light to electricity conversion efficiencies (>10%) in DSC applications (Nazeeruddin et al., 1993; Su et al., 2020). The N719 dye has demonstrated beneficial properties such as; amphiphilic nature, stronger electrostatic binding onto the TiO₂ surface, increased stability and higher oxidation potential that leads to deeper HOMO (highest occupied molecular orbital) energy levels which in turn increases the cell voltage, contributing to high efficiencies (Abdellah and El-Shafei, 2019; Ashraf et al., 2018).

However, dye N719 is only responsive to 500–560 nm wavelengths. Therefore, it was hypothesized that Ag/AgBr's broader spectral response ($\lambda > 400$ nm) would be beneficial for the DSC performance. Additionally, as they will be anchored to a TiO₂ matrix, system would be stable. The incorporation of plasmonic photosensitizers into solar cells provide enhancement in light absorption, scattering cross-section, tunability of light absorption profile, electron traps, and efficient charge carrier separation via LSPR effect, all of which contribute in maximizing the photovoltaic efficiency. The vectorial charge transfer process discussed above was thought to greatly amplify the charge transfer mechanism in the DSC. Therefore, for the first time, and to the best of our knowledge, a well-functioning DSC was fabricated by incorporating Ag/AgBr/TiO₂ nanocomposite in the photoanode, exhibiting enhanced PCE. This is the first report showing that in addition to the well-established photocatalytic nature of the Ag/AgBr/TiO₂ composite, it could also be successfully utilized in dye-sensitized solar cells to optimize their efficiency.

Table 1

The amounts of Ag/AgBr/TiO₂ composite used and final photoanode compositions of the DSCs.

DSC batch no.	Mass of P25 (mg)	Mass of Ag/AgBr/TiO ₂ (mg)	Photoanode composition
B1	250.0	0.0	FTO/P90/P25 _(250.0 mg) & (Ag/AgBr/TiO ₂) _(0.0 mg) /N719
B2	249.5	0.5	FTO/P90/P25 _(249.5 mg) & (Ag/AgBr/TiO ₂) _(0.5 mg) /N719
B3	249.0	1.0	FTO/P90/P25 _(249.0 mg) & (Ag/AgBr/TiO ₂) _(1.0 mg) /N719
B4	248.5	1.5	FTO/P90/P25 _(248.5 mg) & (Ag/AgBr/TiO ₂) _(1.5 mg) /N719
B5	248.0	2.0	FTO/P90/P25 _(248.0 mg) & (Ag/AgBr/TiO ₂) _(2.0 mg) /N719

2. Experimental

2.1. Materials

Analytical reagent grade silver nitrate (AgNO₃ (s), >99.9%) was purchased from BDH. Potassium bromide (KBr, 99+%), sodium dodecylbenzenesulfonate (SDBS, technical grade, cat. no. 289957) and titanium(IV) butoxide (TBOT, reagent grade, 97%) were purchased from Merck. For the photoanode fabrication, titanium dioxide powder TiO₂ P25 was purchased from Degussa AG and Aeroxide TiO₂ P90 powder was purchased from Evonik. Fluorine-doped conducting Tin Oxide (FTO) glass (Solaronix sheet glass 8 Ω sq^{-1}), and ruthenium dye N719 [RuL₂(NCS)₂:2TBA (L = 2,2'-bipyridyl-4, 4'-dicarboxylic acid); TBA = tetrabutyl ammonium] were obtained from Solaronix. Triton X-100 nonionic surfactant (laboratory grade, cat. no. 9002-93-1), poly (ethylene glycol) (PEG, 99.8%, Mw = 1000 g mol⁻¹), and Nitric acid (HNO₃, 69%) were purchased from Merck. Ethanol absolute (anhydrous, > 99.8%) was purchased from VWR Chemicals. For the liquid iodide electrolyte preparation, ethylene carbonate (EC, 98%), tetrapropylammonium iodide (Pr₄NI, 98%), iodine flakes (I₂, > 99%), and acetonitrile (anhydrous) were purchased from Merck. Milli Q water with 18.2 M Ω cm resistivity and 6.998 pH from NIFS laboratory was used for all sample preparation and washing.

2.2. Synthesis of Ag/AgBr/TiO₂ nanocomposite

Ag/AgBr/TiO₂ composite was synthesized in aqueous SDBS media adopting a previously reported method (Boxi and Paria, 2015). In a typical synthesis, AgNO₃ (aq), KBr (aq) solutions were prepared to have 0.1 mM concentrations each in the final solution. They were then mixed in the presence of SDBS under constant stirring. After stirring the solution mixture for 30 min to let AgBr nanoparticle form, it was sonicated in a bath sonicator for 20 min at constant temperature. Then, 100 μ l of titanium(IV) butoxide (TBOT) was slowly added to the mixture under vigorous stirring. After 5 min into TBOT addition, conc. HNO₃ acid was added drop wise to bring the solution pH to 2, and the was kept at constant stirring for another 35 min. The resulting AgBr/TiO₂ composite was then separated by centrifuging at 7000 rpm, and subsequently washed by three successive washing cycles using an ethanol and water mixture of 2 : 1 v/v. Afterwards, the particles were dispersed in Milli Q water and were exposed to normal light conditions for 48 h for formation of Ag NPs. Finally, the Ag/AgBr/TiO₂ composite was separated by centrifugation and was dispersed in absolute ethanol to minimize the Ag/AgBr/TiO₂ composite's contact with atmospheric or dissolved oxygen. A control sample of TiO₂ was synthesized by sol-gel synthesis method using TBOT, in pH = 2 acidic media.

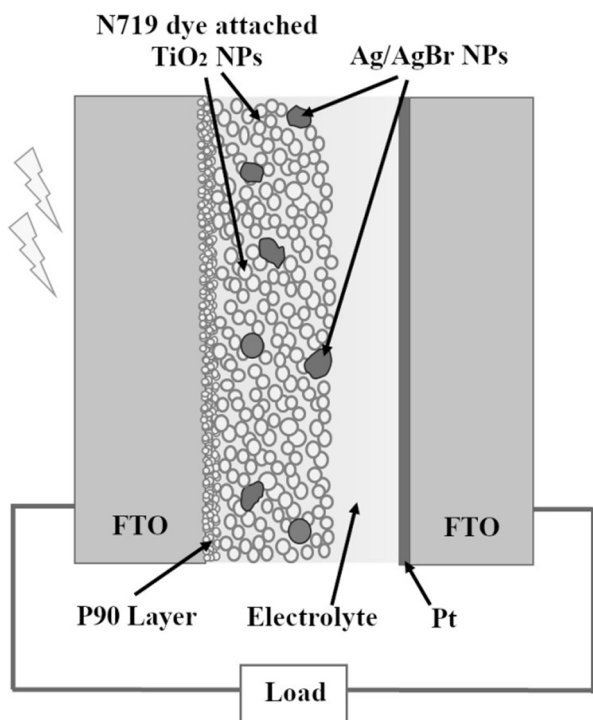


Fig. 1. Schematic diagram of the DSC composed of Ag/AgBr/TiO₂ composite incorporated photoanodes.

2.3. DSC fabrication

2.3.1. Photoanode fabrication

A series of photoanodes were fabricated using P25 TiO₂ powder and different amounts of Ag/AgBr/TiO₂ composite (Table 2.1), using the previously reported HNO₃ method (Kumari et al., 2017). FTO glasses were cut into 1 × 2 cm² rectangular pieces and ultrasonically cleaned by a base, an acid and Milli Q water sequentially, followed by boiling in isopropyl alcohol and drying to ensure a clean surface. For the blocking layer, a P90 TiO₂ paste (0.5 g P90 TiO₂ powder and 2 ml of 0.1 M HNO₃ ground together) was spin coated (3000 rpm) on to pre-cleaned FTOs, followed by sintering at 450 °C for 45 mins.

For a particular batch of DSCs, appropriate amounts (as indicated in Table 1) of TiO₂ powder (Degussa P-25) was grounded using mortar and pestle for 5 mins with 0.5 ml of 0.1 M HNO₃. Appropriate amounts of Ag/AgBr/TiO₂ composite (as indicated in Table 1) dispersion was then added to the P25 paste and grounded thoroughly until a similar consistency was obtained for all five batches. For all DSC batches the total solids weight (P25 weight + Ag/AgBr/TiO₂ composite weight) in the photoanode paste was kept at constant value of 250 mg. Afterwards, 0.5 g of PEG2000 and 0.2 g of TritonX-100 was added to the paste while grinding, followed by another 0.5 ml of 0.1 M HNO₃. The thoroughly ground creamy paste was then doctor bladed on to P90 blocking layer coated FTO glasses. Excess paste was removed to keep the active cell area of 0.25 cm². The FTO/P90/P25_(250-x mg) & (Ag/AgBr/TiO₂)_(x mg) films were then sintered at 450 °C for 45 min and were gradually cooled down to room temperature. Subsequently, the films were dipped in 0.3 mM ethanolic N719 ruthenium dye solution for 24 h at room temperature, and the FTO/P90/P25_(250-x mg) & (Ag/AgBr/TiO₂)_(x mg)/N719 films were washed gently with ethanol and were dried in air before cell assembly. B1 refers to the reference cells fabricated using photoanodes purely composed of P25 TiO₂, whereas B2, B3, B4 and B5 refer to the cells fabricated using photoanodes loaded with 0.5, 1.0, 1.5, and 2.0 mg of the composite, respectively.

2.3.2. Liquid iodide electrolyte

For the preparation of the liquid electrolyte containing the I⁻/I₃⁻ redox couple, 0.738 g of tetra-propyl ammonium iodide (Pr₄NI) and 0.060 g of iodine (I₂) were added to a pre-cleaned vile containing 3.6 ml of melted ethylene carbonate (EC) and 1.0 ml of acetonitrile. The solution was kept under constant stirring overnight.

2.3.3. Cell assembly

As prepared iodide electrolyte was sandwiched between a particular FTO/P90/P25_(250.0-x mg) & Ag/AgBr/TiO₂ (x mg)/N719 photoanode and a Pt counter electrode. The two electrodes were held firmly under gentle pressure together by crocodile clips for cell characterization and measurements. The schematic diagram of the assembled cell with Ag/AgBr/TiO₂ photoanode is illustrated in Fig. 1.

2.4. Characterizations and measurements

2.4.1. Characterization of Ag/AgBr/TiO₂ composites

The crystalline nature of the composite was observed by Bruker D8 Advanced Eco Powder X-ray Diffractometer (0.01° s⁻¹ scanning rate, Cu K_α radiation, λ = 1.5406 Å). Particle size and morphology were observed by transmission electron microscope (TEM) JEOL JEM-2100 and the elemental maps by the energy dispersive x-ray spectroscopy (EDX) with the TEM equipped with EDX (Gatan, USA). Chemical composition of the particles and the valance states were measured by Thermo Scientific TM ESCALAB Xi + X-ray photoelectron spectrometer (XPS). To measure the light absorption spectra UV–Visible spectrophotometer (Shimadzu 2450, λ = 200 nm to 900 nm) was used.

2.4.2. Photoanode characterization and DSC performance

The layered structure of the photoanode was observed by Hitachi SU6600 scanning electron microscope (SEM) cross section analysis. Photon absorption spectra of the photoanode were obtained by UV–Visible spectrophotometer (Shimadzu 2450, λ = 200 nm to 900 nm), where, a thin film of each photoanode paste was spin coated onto pre-cleaned microscope glass slides, at 3000 rpm for 1 min followed by sintering at 450 °C for 45 mins, before the UV–Vis test. The N719 dye loading capacity of the photoanodes (0.25 cm² active cell area) were determined by, first dipping the films in N719 dye for 24 h followed by desorbing the dye of each photoanode for 2 h in 2 ml of 0.1 M NaOH_(aq) solution. The NaOH solutions with the desorbed dye were analyzed for light absorbance with UV–Visible spectrophotometer (Shimadzu 2450 at λ = 495 to 535 nm). With reference to a pre-plotted calibration curve, the amount of dye adsorbed by the semiconductive thin films were calculated. Flat band potential variation of the five semiconductive films were determined by immersing them in a 0.5 M Na₂SO₄ electrolyte solution at pH 7. The stabilized voltage was measured with respect to a standard calomel electrode (SCE) using a Metrohm Autolab PGSTAT 128 N Potentiostat with scanned frequencies of 1.0 kHz and 1.5 kHz.

PCEs and the photocurrent density vs voltage (*J*–*V*) characteristics of the solar cells were measured under the illumination of 100 mW cm⁻² (AM 1.5) simulated sunlight via an Oriel LCS-100 solar simulator (consisting of a 100 W Ozone Free Xenon Lamp) coupled with Metrohm Autolab potentiostat/galvenostat PGSTAT 128 N. The same setup was used for electrochemical impedance spectroscopy (EIS) of the DSC using the FRA 32 M Frequency Response Analyzer (FRA) procedure in a 0.01 Hz to 1 M Hz frequency range. Dark *J*–*V* measurements were obtained under dark conditions with the same Autolab PGSTAT 128 N. A monochromatic light illumination via Bentham PVE300 unit, comprised of TMC 300 monochromator–based IPCE system (150 W Xenon arc lamp, in 300 – 800 nm λ range) was utilized to measure incident photon to current conversion efficiency (IPCE) of the DSCs. The hysteresis of the *J*–*V* curves were obtained by conducting a forward *I*–*V* scan (0–0.8 V) and a reverse *I*–*V* scan (0.8–0 V) at scan rate of 100 mV s⁻¹ for the reference B1 and optimum B3 DSCs. For all of the above measurements, the active cell area was kept at a constant value of 0.25 cm².

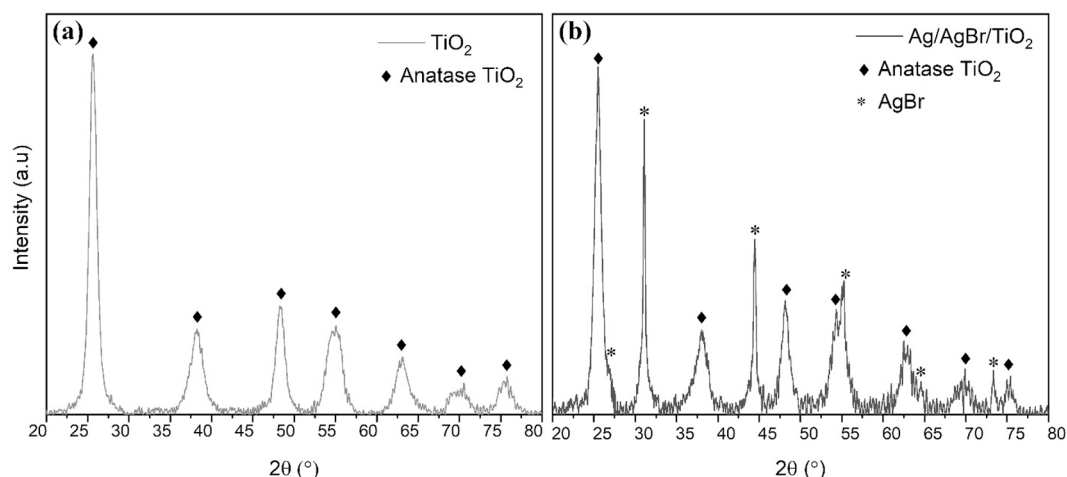


Fig. 2. XRD spectra of (a) Pure TiO₂ sample and (b) Ag/AgBr/TiO₂ composite.

3. Results and discussion

3.1. Synthesis of Ag/AgBr/TiO₂ composite

The presence of the SDBS anionic surfactant was expected to control the growth rate, enhance dispersibility of AgBr and to increase the negative surface charge of the AgBr particles. After addition of TBOT, the solution pH was brought down to 2.0, as, in acidic pH the surface OH groups of TiO₂ clusters protonate and attain a positive surface charge (Suwarnkar et al., 2014), creating a favourable environment for the negatively charged AgBr particles to be loaded onto the TiO₂ matrix as a result of electrostatic attractions. Exposing the AgBr loaded TiO₂ particles to normal light conditions facilitated the metallic Ag clusters formation on the AgBr surface, resulting in the Ag/AgBr/TiO₂ composite.

3.2. Characterization of Ag/AgBr/TiO₂ composite

3.2.1. XRD analysis

Fig. 2 illustrates and compares the X-ray diffraction patterns of the Ag/AgBr/TiO₂ composite and a pure TiO₂ sample. The XRD pattern of Ag/AgBr/TiO₂ composite confirms the presence of AgBr and anatase TiO₂. XRD pattern of pure TiO₂ sample is shown in Fig. 2 (a). Peaks shown at $2\theta = 25.5^\circ, 37.9^\circ, 48.2^\circ, 54.8^\circ, 63.3^\circ, 70.3^\circ, \text{ and } 75.4^\circ$ can be indexed to the (101), (103), (200), (211), (204), (220), and (215) planes of anatase TiO₂, in turn (Li et al., 2017; Suwarnkar et al., 2014). It is noteworthy that the characteristic rutile peaks at 27.3° (111) and 68.6° (301) are absent from both XRD patterns. The use of titanium

butoxide in TiO₂ sol-gel synthesis and sintering at 450 °C favours the formation of anatase phase rather than the rutile phase (D. Wang et al., 2012), which explains the absence of rutile peaks. The characteristic peaks corresponding to cubic AgBr (111), (200), (220), (222), (400), and (420) planes can be identified at $2\theta = 26.6^\circ, 30.9^\circ, 44.4^\circ, 55.0^\circ, 64.5^\circ \text{ and } 73.4^\circ$ respectively, in the XRD spectrum shown in Fig. 2 (b) (Rawal et al., 2013; X. Wang et al., 2012). All peaks corresponding to pure anatase TiO₂ are also present in the composite XRD spectrum. This confirms the co-existence of AgBr and TiO₂ in the composite. It is evident that TiO₂ in both reference and composite samples exist in the pure anatase phase, which is the most preferable phase of TiO₂ for DSC applications due to its higher band gap of 3.2 eV. On the other hand, all three characteristic peaks of Ag⁰, usually found at 38.1° - (111), 44.3° - (200), and 64.7° - (220) (Suwarnkar et al., 2014), overlapped with either TiO₂ or AgBr characteristic peaks found at the same positions. When deconvoluted, two of the three Ag⁰ characteristic peaks could be fitted into double peaks. However, an XPS scan was carried out to confirm the presence of Ag⁰ with certainty.

3.2.2. XPS analysis

To confirm the presence of metallic silver species and to understand their chemical status, further testing was carried out using the XPS technique. The Fig. 3 (a) demonstrates the survey scan XPS spectrum and Fig. 3 (b) shows the high resolution XPS spectrum of the Ag 3d region. The survey scan proves the presence of all four elements under consideration; titanium (Ti), oxygen (O), silver (Ag) and bromine (Br) (Gan et al., 2019). To prove the chemical statuses of silver, a high

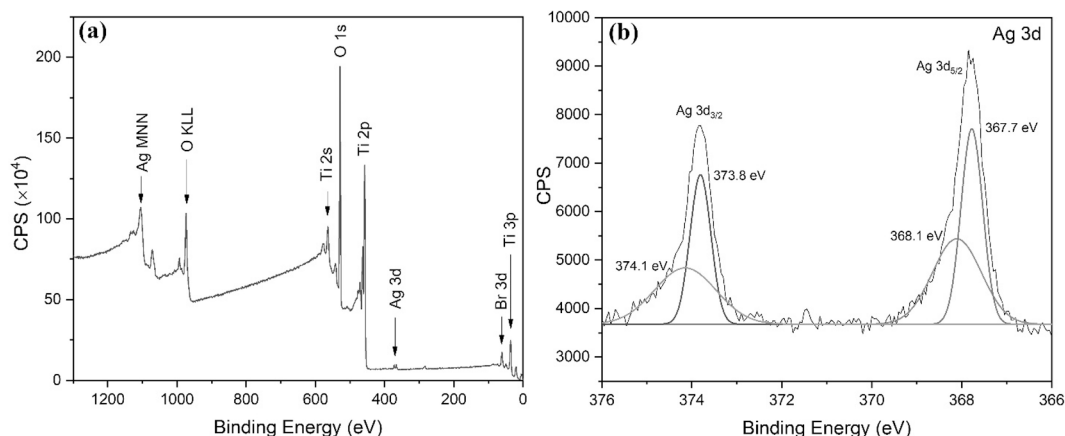


Fig. 3. XPS spectra of (a) survey scan and (b) Ag 3d region.

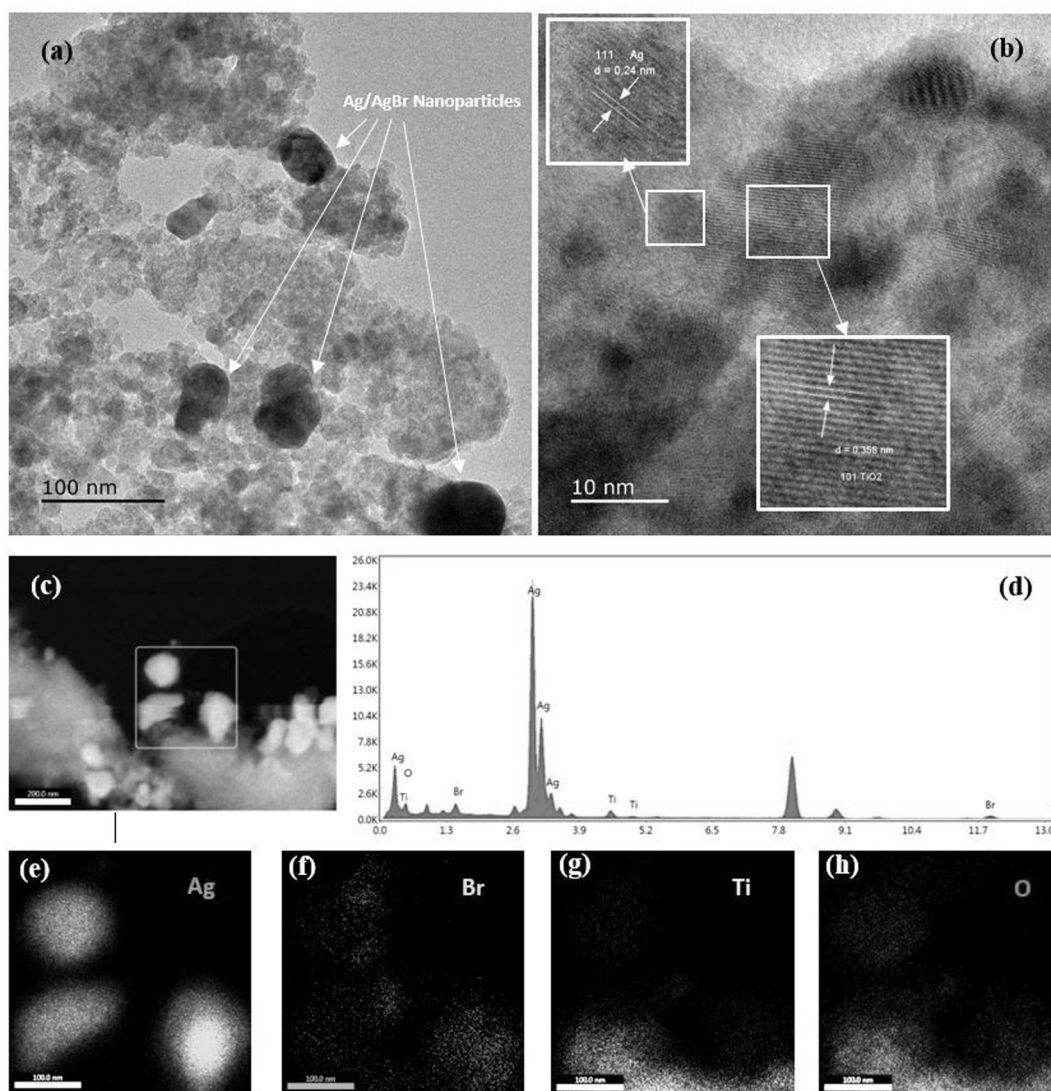


Fig. 4. (a) TEM image of the Ag/AgBr doped TiO₂ composite, (b) HRTEM image of the composite, (c) area of the composite chosen for EDX analysis, (d) the elemental composition spectrum, and elemental maps of (e) silver, (f) bromine, (g) titanium, and (h) oxygen of the selected area.

resolution XPS analysis in the Ag 3d region was obtained. Two bands can be observed in Ag 3d XPS spectrum at 367.9 eV and 373.8 eV, that can be indexed to Ag 3d_{5/2} and Ag 3d_{3/2} binding energies, respectively (Gan et al., 2019). The said two bands can be further fitted into two sets of double peaks, as shown in Fig. 3 (b).

The peaks at 368.1 eV and 374.1 eV can be attributed to the Ag 3d_{5/2} and Ag 3d_{3/2} of metallic Ag (Ag⁰), in that order (Hou et al., 2011; X. Wang et al., 2012), which solidify the existence of metallic silver in the Ag/AgBr/TiO₂ composite. The peaks found at 367.7 eV and 373.8 eV corresponds to the Ag 3d_{5/2} and Ag 3d_{3/2} binding energies of Ag⁺ species (Hou et al., 2011; X. Wang et al., 2012). This confirms the presence of AgBr in the sample. Furthermore, it could be observed that the peaks corresponding to Ag⁺ show higher intensity than the Ag⁰ peaks. It can be safely stated that both metallic Ag and AgBr co-exists in the sample, whereas AgBr appears to be the predominant species.

3.2.3. TEM, HRTEM and EDX analysis

Fig. 4 depicts the results of TEM, HRTEM and EDX analyses. The TEM image (Fig. 4 (a)), shows how the Ag/AgBr nanoparticles are loaded onto the TiO₂ matrix. Particle sizes of the Ag/AgBr nanoparticles seem to be present in varied sizes and shapes but are observed to be less than 100 nm of diameter. The TiO₂ matrix appears to be composed of roughly

10 nm or lower sized particles. Fig. 4 (b) shows an HRTEM image of the sample. The lattice patterns highlighted in squared areas correspond to metallic silver (111) plane with 0.24 nm d spacing, and TiO₂ (101) plane with 0.358 nm d spacing (Gan et al., 2019; Suwarnkar et al., 2014; Wang et al., 2015; X. Wang et al., 2012). However, characteristic lattice patterns could not be identified for AgBr in the HRTEM analysis. The high energy electron beam used in the TEM and HRTEM analysis might have accelerated the decomposition of AgBr nanoparticles resulting in metallic silver (D. Wang et al., 2012).

Fig. 4 (c), and Fig. 4 (d) show a selected area and its elemental composition spectrum, respectively. The EDX tests show the existence of the elements Ti, O, Ag, and Br, which is consistent with both XPS and XRD characterizations, although, the elemental map for Br showed feeble intensity, insinuating the decomposition of AgBr nanoparticles. Nevertheless, in general, even the traces of Br can be found at the specific areas where element Ag exists, in the elemental maps given in Fig. 4 (e) and (f) for Ag and Br, thus confirming the position of AgBr particles in the TiO₂ matrix. Ti and O elements exists in the same areas, indicating the position and existence of TiO₂. All tests; XRD, XPS, TEM, HRTEM and EDX provide consolidative proof of the co-existence of Ag⁰, AgBr, and TiO₂ in the composite sample.

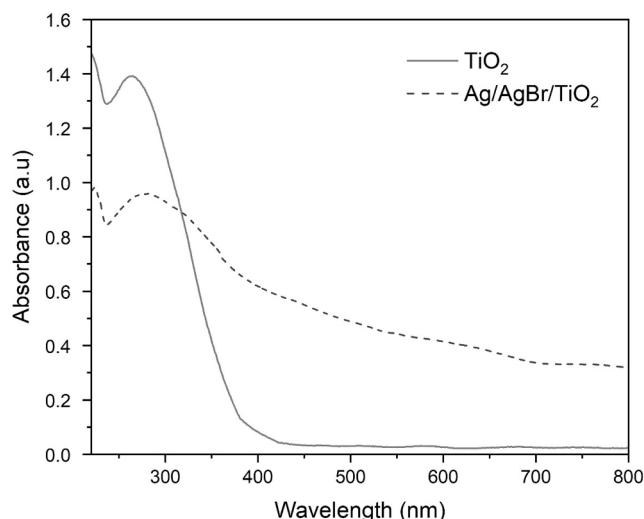


Fig. 5. UV–VIS spectra of pure TiO_2 and Ag/AgBr/TiO_2 composite samples.

3.2.4. UV–Visible spectroscopic analysis

As the Ag/AgBr/TiO_2 nanocomposite is incorporated into DSC photoanodes as photosensitizers the photoresponse of the composite photoanode is of utmost importance. Fig. 5 compares the optical response of the composite with that of pure TiO_2 . The UV–Vis spectrum of pure TiO_2 has its characteristic exciton absorption band maxima at $\lambda = 265$ nm in the UV region (Hong et al., 2013). However, it can be seen that its absorption edge has red shifted towards 400 nm wavelength region. During the sintering process, many oxygen vacancies are formed on the TiO_2 surface and these defective structures absorb visible region photons, red shifting the absorption edge according to X. Wang et al. (2012). In comparison, Ag/AgBr/TiO_2 composite's spectrum exhibits strong optical absorption throughout the visible region approximately from 400 nm to 800 nm wavelengths. The enhanced optical absorption in the visible region is evidently due to the local surface plasmon resonance (LSPR) effect by Ag NPs which is originated by the collective oscillations of

electrons in the Ag nanoparticles stimulated by optical excitations. At the same time, Ag^+ ions from AgBr gets incorporated into the TiO_2 lattice (similar to doping by N, S already reported) and causes energy band narrowing. The red shift observed in the optical absorption edge can be attributed to this energy band gap narrowing (Hamrouni et al., 2020). AgBr with an indirect bandgap of 2.6 eV is also expected to contribute to the strong absorption in the visible region as well. This enhanced visible light absorption due to the nanocomposite was exploited in fabricating the efficiency enhanced DSCs discussed under this project. Similar absorption spectra have been observed for this composite in previous studies (Hu et al., 2006; X. Wang et al., 2012; Yu et al., 2009). In order to determine the Ag/AgBr/TiO_2 nanocomposites ability to be used as a co-sensitizer with N719 dye in DSCs further tests were carried out for the composite incorporated photoanodes and DSCs.

3.3. Characterization of the Ag/AgBr/TiO_2 doped P25 photoanode

3.3.1. SEM cross-sectional analysis

The layered structure of the photoanode before the dye sensitization is shown in the SEM micrograph given under Fig. 6. The photoanode is composed of 3 initial layers; (1) FTO layer with ≈ 0.6 μm average thickness, (2) ≈ 0.2 μm thick P90 TiO_2 compact layer, and (3) Ag/AgBr/TiO_2 composite loaded P25 TiO_2 layer which is of ≈ 11 μm thickness on an average. The FTO acts as the electron collector, while the P90 compact layer physically shields the FTO layer from the electrolyte and hinders the recombination of photogenerated electrons in the FTO with the oxidized species in the electrolyte effectively minimizing dark currents (Musila et al., 2018). The third layer provides the base for dye adsorption. It should be thick enough for the maximum dye adsorption as well as thin enough for the incident photons to efficiently penetrate the full depth of the active layer. The optimum thickness of the active TiO_2 layer reported by a previous study of our group is around ≈ 12 μm which is in good agreement with the active layer thicknesses of the fabricated DSCs under this study (Kumari et al., 2016).

3.3.2. UV–VIS spectroscopic analysis of the photoanodes

The photoresponse of the pure P25 and Ag/AgBr/TiO_2 incorporated P25 photoanodes without the dye layer were investigated by UV–Vis

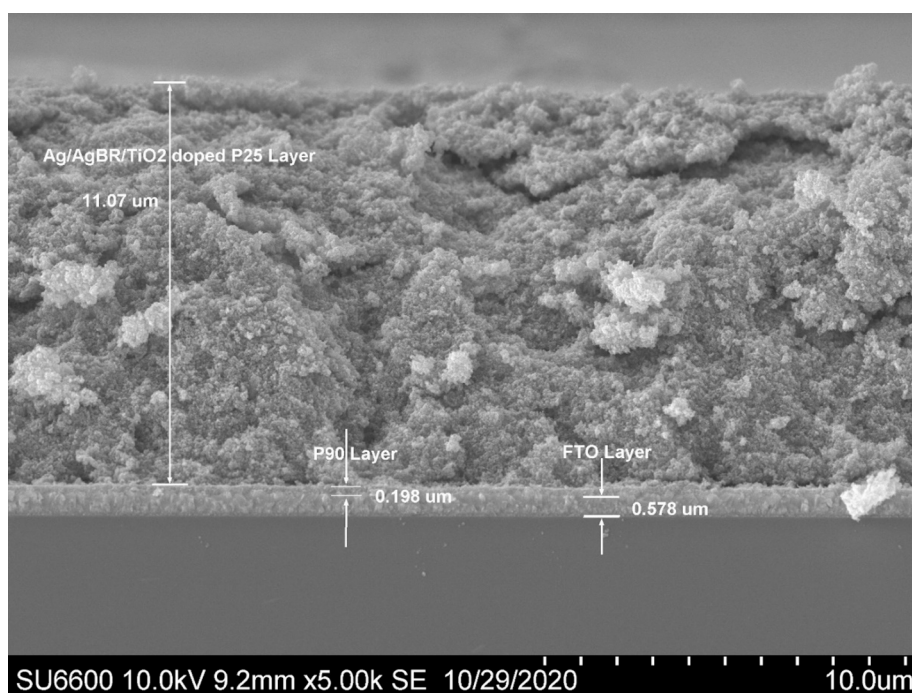


Fig. 6. SEM image of the cross-section of the photoanode.

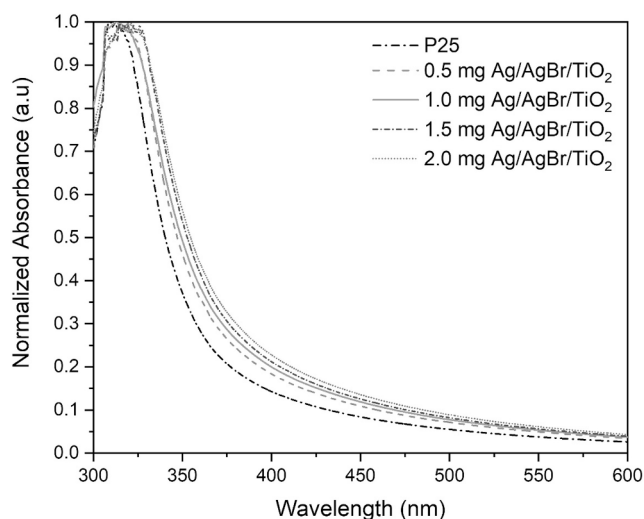


Fig. 7. Normalized UV–VIS absorption spectra corresponding to pure P25 and other photoanodes doped with different amounts of Ag/AgBr/TiO₂ composite.

spectrometer. As depicted in Fig. 7 the absorption edges and absorption peak maxima can be seen as red shifted with the increased amounts of Ag/AgBr/TiO₂ composite. AgBr semiconductor with an inherent bandgap of 2.6 eV, absorbs light around 470 nm wavelengths (Gan et al., 2019; Hu et al., 2006). Metallic silver clusters present in the composite gives rise to localized surface plasmon resonance, which is originated by the collective oscillations of electrons in the Ag nanoparticles stimulated by optical excitations. The enhanced optical absorption in the visible region is evidently due to the incorporation of AgBr and LSPR effect due to Ag nanoparticles. The red shift observed in the absorption spectra is very likely due a downward shift in the conduction band and/or an upward shift in the valence band, which leads to a decrease in the energy band gap value of the composite photoanode due to the presence of Ag/AgBr. The doping of Ag⁺ present in the composite, into the TiO₂ lattice introduce intermediate energy states in the forbidden energy gap of TiO₂, due to strong electron coupling between silver and the TiO₂ orbitals resulting in a reduction of the energy gap (Hamrouni et al., 2020).

The bandgap energy (E_g) values of the photoanodes were calculated using Tauc's plots where, 3.55 eV, 3.50 eV, 3.47 eV, 3.43 eV, and 3.41 eV E_g values were obtained for B1, B2, B3, B4, and B5 photoanode respectively, which confirms the reduction in the energy gap with higher composite incorporation amounts. Similar band gap narrowing due to doping and Ag Nps have been observed and quantitatively estimated by Su Pei Lim et al for the DSSC system made with Ag NP-Decorated N,S-Co-Doped-TiO₂ photoanodes (Lim et al., 2015).

3.3.3. Mott-Schottky measurements

This technique is an effective way to determine the flat-band potentials of an active semiconductor material used for DSC photoanodes. For a particular photoanode, Mott-Schottky plots were obtained at two different frequencies (1 kHz and 1.5 kHz) for accuracy. Fig. 8 illustrates such obtained curves and their x intercepts of the gradients for all five photoanodes under consideration. The flat-band potential values (V_{fb}) of each photoanode is summarized in Table 2.

According to Fig. 8, the accumulation happens at potentials more negative than the flat-band potential, confirming n-type nature of both pure and composite incorporated photoanodes (Pastor-Moreno and Riley, 2002; Zhang, 2005). This is obviously expected as both TiO₂ and AgBr are n-type semiconductors. The flat-band potential should always be lower than the conduction band edge of a semiconductor (TiO₂ CB edge = -0.5 V vs NHE) (Li et al., 2014; Rawal et al., 2013). Not only this is true for the semiconductors under consideration, but it could also be observed that the V_{fb} is much closer to the CB edge rather than the VB

edge (2.7 V vs NHE) of TiO₂ (Li et al., 2014; Rawal et al., 2013), further solidifying the n-type characteristics of the active material. Interestingly, the V_{fb} of differently composed photoanodes shows roughly similar values. The synergetic effects of photosensitive AgBr semiconductor and metallic Ag nanoparticles seem to have no significant net effect in the V_{fb} of photoanodes. A possible reasoning for this behavior is presented in J - V characteristic analysis, in agreement with observed open circuit voltages (V_{oc}) variation.

3.3.4. N719 Dye loading capacity of the photoanodes

The amount of dye loaded onto the semiconductor is a PCE determining factor. The amounts of dye adsorbed by the pure and modified photoanodes are listed in Table 3. Unfortunately, the dye adsorption capacity of the photoanodes has reduced with the increasing amounts of Ag/AgBr/TiO₂ composite, incorporated in the P25 photoanode showing the highest N719 dye adsorption of 1.15 $\mu\text{M cm}^{-2}$. The available space for N719 dye attachment in the photoanode may have reduced with the increasing amounts of Ag/AgBr. A possible reasoning is as follows. AgBr predominantly shows Frenkel defects in their lattice. On AgBr surface, the vacancy formation is reported to be much higher than interstitials formation. Thus, as the predominant defects, vacancies fix the surface charge of AgBr as negative (Bose and Govindacharyulu, 1980). The adsorption of the N719 dye onto the semiconductor surface is due to the carboxyl ($-\text{COO}^-$) groups which are also negatively charged. It can be assumed that due to these like charge repulsion, dye attachment in the AgBr containing photoanodes is less than that of the reference photoanode, which is not a favourable situation as lower dye loading would decrease the photocurrent. However, as explained in the following sections, Ag/AgBr/TiO₂ composite has indeed enhanced the photocurrent, even at the expense of lower dye loadings.

3.4. Photovoltaic performance of the dye-sensitized solar cells

To analyze the photovoltaic performance of the DSCs made with the composite incorporated photoanodes, the photocurrent density vs voltage (J - V) curves, incident photon to current conversion variation (IPCE), electrochemical impedance data, and dark current variations were obtained. J - V characteristics were measured under simulated sunlight illuminated at 100 mW cm^{-2} (AM 1.5) for all cells. J - V curves plotted in Fig. 9 (a) shows that all four DSCs with Ag/AgBr/TiO₂ composite photoanodes have higher photocurrent densities (J_{sc}), compared to the reference cell (B1). The highest J_{sc} of 18.78 mA cm^{-2} has been obtained for the DSC with 1.0 mg optimal weight of the composite in its photoanode. J_{sc} gradually increases from the reference cell to the optimum cell (B3), and then reduces again with the increasing amounts of Ag/AgBr/TiO₂ composite. This variation in photocurrent is consistent with the IPCE measurements as shown in Fig. 9 (b). In agreement with flat-band potentials of the photoanodes the open circuit voltages (V_{oc}) of the modified DSCs do not show a considerable variation compared to the reference cell's V_{oc} . All the cells exhibit V_{oc} values around ≈ 710.0 mV. The fill factors (FF) also show no significant variation. On the other hand, the PCEs of the DSCs follow the trend demonstrated by J_{sc} values suggesting that the PCE enhancement is predominantly caused by the increase in the concentration of photogenerated electrons in the composite photoanode. The PCE values of the cells have dramatically increased from 6.45% for the reference cell up to 8.46% for the DSC fabricated with 1.0 mg Ag/AgBr/TiO₂ composite, which also shows the maximum J_{sc} value. In agreement with the variation of J_{sc} , all PCE values of the modified DSCs are higher than that of the reference cell. A quantitative summary of the photovoltaic parameters measured and calculated by the J - V analysis is given in Table 4.

The higher photocurrent generation in the Ag/AgBr/TiO₂ carrying cells could be assigned to several possible mechanisms. The increased photoelectron generation by AgBr nanoparticles alongside the N719 dye photoelectron excitations, could be one such mechanism (Hou et al., 2011; Xue et al., 2016; Yu et al., 2009). Upon illumination by the

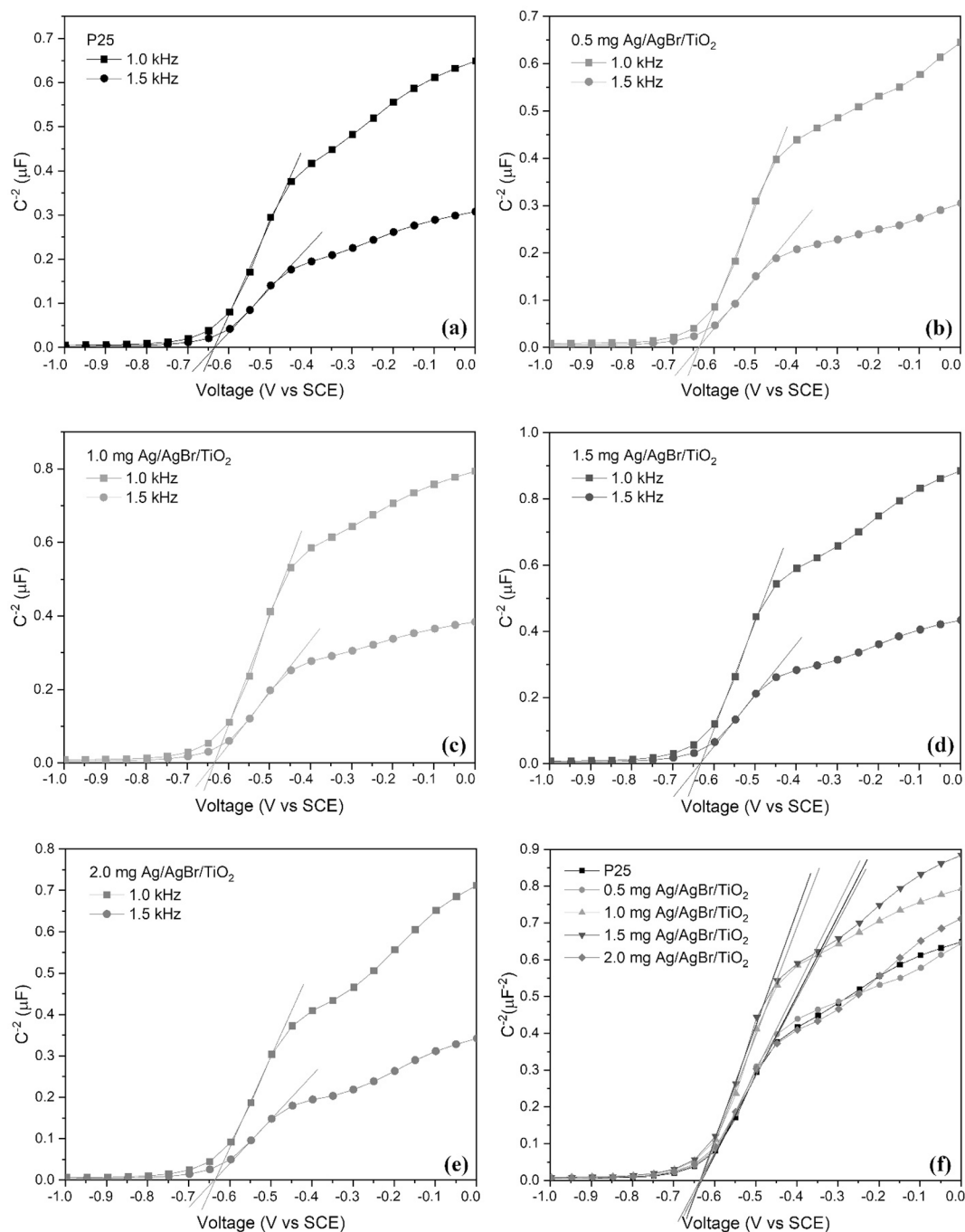


Fig. 8. The Mott-Schottky plots of (a) B1, (b) B2, (c) B3, (d) B4, (e) B5 photoanodes at 1.0 kHz and 1.5 kHz, (f) Mott-Schottky plots of all photoanodes at 1.0 kHz.

resonant λ_s , the induced LSPR effect from the Ag NPs would enhance the electric field in their immediate vicinity. These intense localized EM fields can further excite the dye and AgBr to produce more electron-hole pairs, whilst contributing to efficient spatial separation of charges and electron conduction through the semiconductor matrix (Dissanayake et al., 2016; Dong et al., 2019; Li et al., 2011). The oscillations in the EM fields separate the photogenerated electrons from AgBr and dye, and accelerate their injection into the TiO₂ CB (Hou et al., 2011; Moskovits, 2011; Yu et al., 2009; Zhang et al., 2017). In addition, LSPR effect results in higher optical absorption and scattering, leading to dramatically increased optical excitations. All these facts appear to contribute to the observed enhancement in the J_{sc} . Hence, with the increment in the J_{sc} , the corresponding PCEs of the composite incorporated DSCs have increased.

Ag NPs are also known to introduce energy states in the forbidden energy gap of the semiconductor. While these forbidden energy states promote low energy photon absorption and quick photogenerated charge injection to TiO₂ from AgBr and dye, they can also act as recombination centers (Hu et al., 2017). The electron lifetimes calculated by bode phase plots of EIS measurements and the dark current analysis results are in very good agreement with this reasoning. Additionally, the decreasing amounts of N719 dye loading may also be a contributing factor for efficiency reduction at higher composite loading than 1.0 mg. Another possibility discussed in previous studies is the higher energy generated in modified cells partly getting converted to heat when higher amounts of photosensitive materials are present (Dong et al., 2019; Li et al., 2017). In addition to the favourable mechanisms that enhance the photocurrent and the PCEs, with the limitations set by

Table 2

Flat-band potential values of the differently composed photoanodes w.r.t SCE and NHE

Batch	Mass of Ag/AgBr/TiO ₂ (mg) in the photoanode	Flat-band potential (mV)	
		vs SCE	vs NHE
B1	0.00 (Pure P25)	-635.7 ± 0.2	-391.7 ± 0.2
		-632.1 ± 2.2	-388.1 ± 2.2
B2	0.50	-632.7 ± 3.1	-388.7 ± 3.1
		-634.1 ± 3.6	-390.1 ± 3.6
B3	1.00	-635.2 ± 5.2	-391.2 ± 5.2

Table 3

Amount of dye loading on the photoanodes

Batch	Mass of Ag/AgBr/TiO ₂ (mg) in the photoanode	Adsorbed dye (μM cm ⁻²)
B1	0.00 (Pure P25)	1.150
B2	0.50	1.072
B3	1.00	0.995
B4	1.50	0.922
B5	2.00	0.734

these competing mechanisms, there seems to exist an optimum loading of 1.0 mg (0.4% wt) of the Ag/AgBr/TiO₂ composite that gives a maximum J_{sc} and a PCE. Then, as the composite loading exceeds this optimum value, the J_{sc} and the subsequent the PCE decrease, may be due to the prominence of the competing mechanisms discussed.

The V_{oc} values of the cells are in good agreement with the flat-band potential measurements, where roughly similar values were observed with different amounts of the composite material in the photoanode. The V_{oc} of a DSC is the potential difference between the quasi-fermi level of the semiconductor and the redox potential of the redox couple. The quasi-fermi level of electrons (E_{fn}) of a semiconductor can be derived with Eq. (1). Here, E_c , n , and N refers to conduction band energy, density of electrons, and density of states available for electrons in the semiconductor, respectively as given by the equation,

$$E_{fn} = E_c + kT \ln \left(\frac{n}{N} \right) \quad (1)$$

Incorporating Ag plasmonic nanoparticles have been reported to reduce V_{oc} of DSCs with some plausible reasoning (Dissanayake et al., 2016; Du et al., 2012; Li et al., 2011). Ag nanoparticles introduce more inhabitable energy states for the photogenerated electrons and as they are physically in contact with TiO₂, the electrons get distributed among

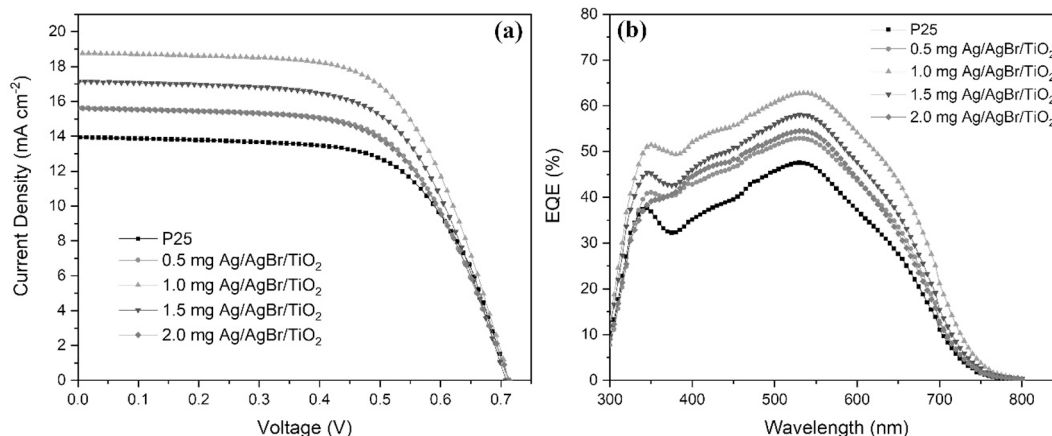
both TiO₂ and Ag MNPs. This effect has been thought to reduce the n/N ratio and in turn the shift the E_{fn} causing V_{oc} reduction. However, when the Ag/AgBr/TiO₂ containing photoanodes are under illumination, the photoexcited electrons of the both AgBr and the dye can be injected to Ag and TiO₂ simultaneously. Ag nanoparticles could accumulate a lot of electrons on their surfaces due to LSPR effects (Lim et al., 2015). There by, the Ag nanoparticles and TiO₂ may accumulate a high density of electrons (n). Thus, even though the available density of states (N) is higher in the semiconductor due to Ag, there can be a higher density of electrons as well, which may result in rising of both n and N . In view of all above possibilities, it could be safely assumed that the n/N ratio may remain roughly constant at the composite loadings under consideration, eventually resulting in approximately similar V_{oc} values. Similar results with essentially similar V_{oc} values have been obtained by other researchers for modified photoanodes (Krishnapriya et al., 2021; Li et al., 2017; Rho et al., 2018).

To verify the trend of photocurrent density observed in J - V measurements IPCE or incident photon to current conversion efficiency spectra of the fabricated pure and doped DSCs were obtained (Fig. 9 (b)). They are a demonstration of how well a solar cell converts incident light at different λ s, to photocurrent. The IPCE of the composite containing photoanodes have been significantly improved in the entire wavelength range. Specifically, in the 400–500 nm and in the 550–700 nm ranges, the Ag/AgBr/TiO₂ composited doped cells show enhanced light harvesting efficiencies. The higher incident photon to electron conversion in the 400–500 nm region can be due to the presence of AgBr narrow bandgap semiconductor. The LSPR effects may be the reason for the enhancement of IPCE in the 550–700 nm visible region (Dissanayake et al., 2016; Li et al., 2011). The maximum IPCE exhibited by the reference cell is 47.55% at 530 nm wavelength. At 0.5 mg composite incorporation the peak IPCE value appears at 530 nm as well. At higher

Table 4

Photovoltaic parameters of the dye-sensitized cells with varying composite photoanode compositions

Batch	Mass of Ag/AgBr/TiO ₂ (mg) in the cell	V_{oc} (V)	J_{sc} (mA cm ⁻²)	FF	η (%)
B1	0.00 (Pure P25)	0.713 ± 0.005	13.95 ± 0.07	0.64 ± 0.01	6.45 ± 0.02
		0.710 ± 0.007	15.63 ± 0.09	0.63 ± 0.01	7.03 ± 0.07
B2	0.50	0.712 ± 0.008	18.78 ± 0.11	0.63 ± 0.01	8.46 ± 0.09
		0.708 ± 0.010	17.18 ± 0.16	0.63 ± 0.01	7.64 ± 0.11
B3	1.00	0.714 ± 0.011	15.62 ± 0.22	0.62 ± 0.01	6.93 ± 0.17

**Fig. 9.** (a) J - V curves, and (b) IPCE variations of DSCs incorporated with different amounts of Ag/AgBr/TiO₂ composite.

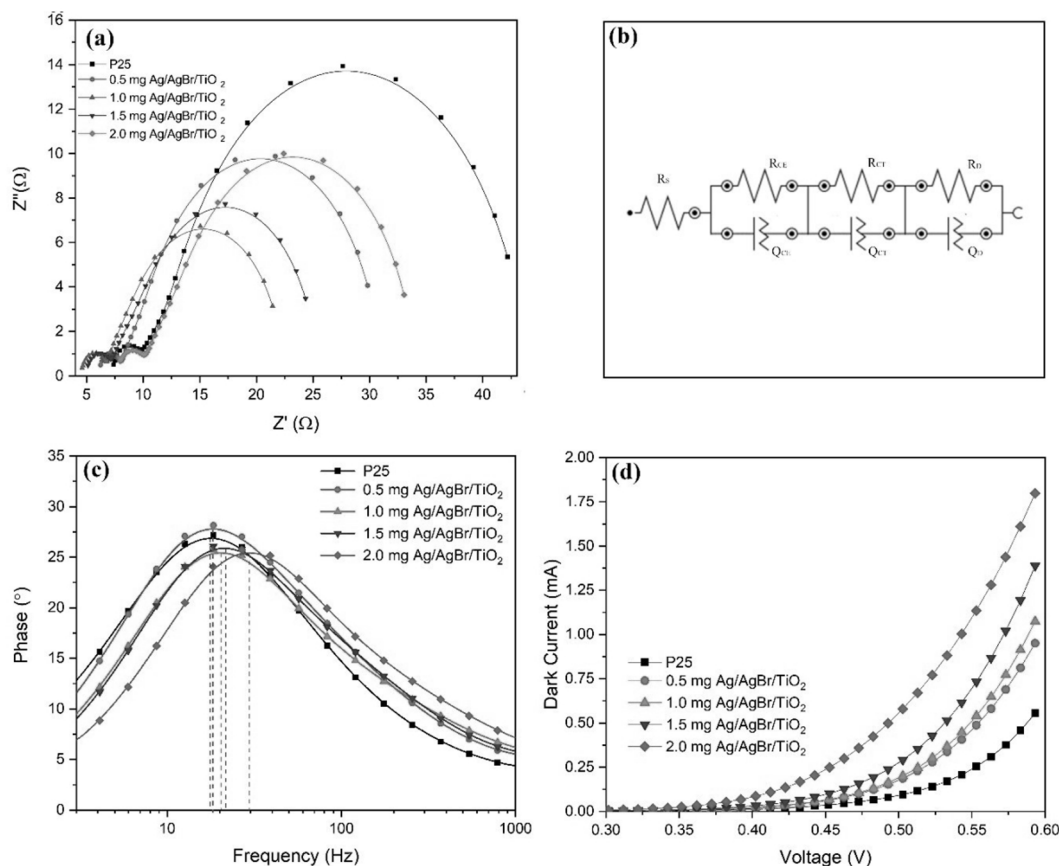


Fig. 10. (a) Nyquist plots under 100 mW cm^{-2} , 1.5 A.M illumination (b) equivalent circuit used for EIS data analysis, (c) Bode phase plots, and (d) dark I-V variation of DSCs incorporated with different amounts of Ag/AgBr/TiO₂ composite.

composite weights, the maximum peak has shifted to 535 nm. Similar peak shifts have been observed for plasmonic material doped DSCs in other studies as well (Dissanayake et al., 2016). This peak IPCE red shift, is in agreement with the red shift observed in the absorption edge of TiO₂ shown in the UV-Vis absorption spectra of the photoanodes. Hence, could be assigned to the reduction in the energy gap of the semiconductor at higher composite loadings, due to the Ag⁺ ions from AgBr getting incorporated into the TiO₂ lattice promoting lower energy photon absorption (Hamrouni et al., 2020).

The highest overall light harvesting ability is seen in the B3 optimized cell with 1.0 mg composite loading, which also correspond to the highest J_{sc} and PCE. The peak IPCE of this cell is 62.77%. At higher composite loading, the peak IPCE decreases gradually.

Area under a particular IPCE curve is proportional to the J_{sc} generated by the respective solar cell as can be seen from Eq. (2).

$$J_{sc} = \frac{hc}{q} \int_{\lambda_1}^{\lambda_2} \frac{P_{1.5AM} \times IPCE(\lambda)}{\lambda} (d\lambda) \quad (2)$$

where h is the Planck's constant ($J \text{ s}^{-1}$), c is the speed of light in vacuum (m s^{-1}), q is the charge of electron, $P_{1.5AM}$ is the radiation flux at AM 1.5 (100 mW cm^{-2}). λ_1 and λ_2 are the limits of the active spectrum. The areas under the IPCE curves of the pure and composited mixed DSCs increase and decrease in the following order; P25 < 0.5 mg < 1.0 mg > 1.5 mg > 2.0 mg loaded solar cells. Also, the IPCE curves of 0.5 mg and 1.5 mg composite incorporated cells show almost similar areas under them. Thus, it can be seen that the J_{sc} variation trend shown by J - V curves is in good agreement with the photocurrent densities obtained from IPCE studies.

Electrochemical impedance spectroscopy (EIS) is a powerful technique that reveals information on charge transport mechanisms inside

an electrochemical system. This technique has been widely exploited in solar cells for determination of charge transport and recombination mechanisms. The Nyquist plots of the Ag/AgBr/TiO₂ composite carrying and pure DSCs under illumination, are illustrated in Fig. 10 (a). Each Nyquist plot showed only two semicircles. The smaller semicircle in the high frequency range represents the charge transfer resistance at the interface of the Pt counter electrode/electrolyte, denoted as R_{CE} and the larger semicircle in the low frequency range is attributed to the charge transfer resistance at the photoanode/electrolyte interface, denoted by R_{CT} . The series resistance R_S can be found on the x axis at the high frequency cut-off of the smaller semicircle (Dissanayake et al., 2016; Hwang et al., 2017). Resistance values were obtained by fitting the impedance data to the equivalent circuit model given in Fig. 10 (b) where, under illuminated conditions, the overall charge transport resistance at the TiO₂/electrolyte interface is labeled as R_{CT} , the resistance at Pt/electrolyte interface is denoted as R_{CE} , whereas R_D is related to the impedance of redox species diffusion in the electrolyte. R_S symbolizes the series resistance of the device.

It is evident that the charge transfer resistance of the P25 DCS reigns the highest, as it owns the largest semicircle in the low frequency region. It is basic knowledge that the impedance and current is inversely proportional. The increasing composite amounts up to 1.0 mg, has gradually reduced the charge transfer resistance, hinting at increasing photocurrents. Following exactly the same trend presented for J - V and IPCE analysis, composite amounts more than 1.0 mg, shows gradual reduction in photocurrent suggesting inefficient electron transfer mechanisms. Thus, the assumptions made on the increased recombination at higher Ag/AgBr/TiO₂ composite loading, may hold true with regards to the charge transfer resistance variation trend as well. Similar variations for plasmonic DSCs have been observed by other researchers (Bai et al., 2020; Hwang et al., 2017). The lowest charge transfer

Table 5

The PCEs, resistance values, frequency maxima and electron lifetimes of the DSCs

Batch	Amount of composite in DSC (mg)	η (%)	R_{CT} (Ω)	R_{CE} (Ω)	f_{max} (Hz)	τ_n (ms)
B1	0.00 (Pure P25)	6.45	31.5	2.47	17.599	9.04
B2	0.50	7.03	20.4	2.52	18.259	8.72
B3	1.00	8.46	13.2	2.34	20.172	7.89
B4	1.50	7.64	15.2	2.82	21.173	7.52
B5	2.00	6.93	20.7	3.46	29.276	5.44

resistance at semiconductor/electrolyte interface was observed for the 1.0 mg composite containing cell with $R_{CT} = 13.2 \Omega$, which is a significant reduction compared to the $R_{CT} = 31.5 \Omega$ of the reference P25 DSC. This clearly shows that the efficient charge transfer mechanisms is caused by the Ag/AgBr/TiO₂ heterostructure and the electron mediator centers (Ag⁰) in the composite TiO₂ photoanode. On the other hand, R_{CE} values do not show a significant variation. The same iodide/tri iodide electrolyte and Pt plate used for all DSC fabrication may have caused unaffected R_{CT} values. The bode phase plots of the DSCs were also plotted to extract information on recombination and electron lifetimes, and are depicted in Fig. 10 (c).

The maximum frequency (f_{max}) of the mid peak in a bode phase plot is inversely proportional to the electron lifetime (τ_n) as shown in Eq. (3). Hence, f_{max} is directly proportional to recombination rate, and sometimes referred to as the recombination frequency (Sarker et al., 2014).

$$\tau_n = \frac{1}{2\pi f_{max}} \quad (3)$$

Interestingly, all the doped photoanodes show higher f_{max} values than that of the reference ($f_{max} = 17.6$ Hz). It is clear that the recombination rates in these composite containing cells are higher than the reference cell. Plasmonic Ag particles, while contributing to efficient electron mediation between the heterojunctions, may also contribute to recombination due to energy levels they induce in the forbidden gap of the semiconductor. Hence, the increasing recombination rates at higher loadings of Ag particles. To further support this idea, electron lifetimes were also calculated and are tabulated in Table 5 with the resistance values and frequency maxima.

The derived electron lifetimes reduce at increased composite loading, which is in support of the claims made above. However, the charge transfer resistance has also obviously reduced when doping weight percentages are increased up to 1.0 mg and subsequently increased again when the composite weight was increased beyond 1.0 mg, which is in good agreement with the photocurrent, IPCE and PCE variation. Reductions in charge transfer resistances of the composite in comparison to P25 matrices have been reported by Xue et al. (2016), where Ag/AgBr/TiO₂ is used as a photocatalytic material. The researchers attribute this reduction in resistance to the efficient charge generation and separation and lower charge diffusion resistance inside the heterostructure. A possible mechanism which supports all parametric variation trends can be elaborated as follows. When illuminated, the ultimately collected photogenerated charge (photocurrent) is a superposition of many mechanisms that happen inside the DSC. Observed photocurrent strongly depends on the rate of photoelectron generation, injection, diffusion, collection and also recombination. It could safely be assumed that a trade-off between charge generation, injection, diffusion with respect to recombination, results in higher photocurrents in the composite photoanode based DSCs. In all these cells the charge generation, injection and diffusion must be superior to corresponding recombination rates. In the P25 cell, even though there is less recombination, the photogenerated electron density must also be low. This claim, validates the rise and fall of the J_{sc} , PCE, IPCE, and also explains the decrease and subsequent increase in the charge transfer resistance at the photoanode, and the existence of an optimum composite loading amount.

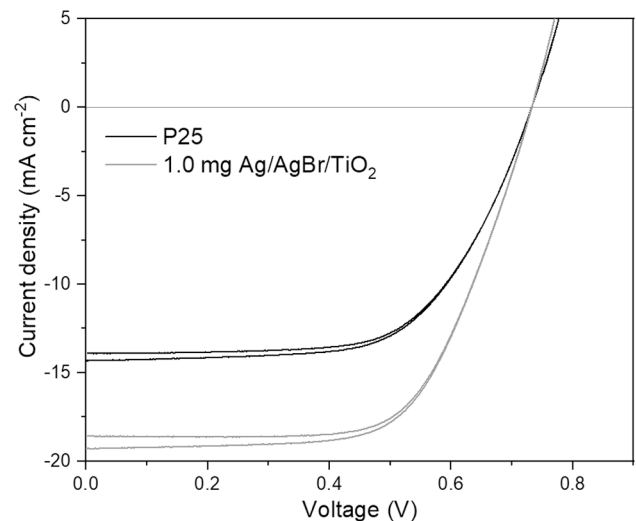


Fig. 11. Hysteresis behavior of the J-V curves of the P25 and 1.0 mg Ag/AgBr/TiO₂ incorporated photoanode containing DSCs.

To further verify the recombination mechanism, a dark *I-V* analysis was conducted. The main reason for the dark current in a DSC is the recombination of the electrons in semiconductor with the redox species in the electrolyte, which is independent of incident photons. When there is no illumination the DSC acts as a typical diode, which is evident from the dark *I-V* curves obtained (Fig. 10 (d)). In consistent with other observations, the higher dark currents are observed in the Ag/AgBr/TiO₂ composite loaded solar cells at forward bias. As expected, the lowest dark current is observed in the pure P25 photoanode containing DCS, an indication of lowest recombination rates. The dark currents have increased for the doped DSCs containing 0.5 mg, 1.0 mg, 1.5 mg and 2.0 mg composite in that order, indicating increasing recombination rates. The dark currents in a diode (or solar cell in the dark) is generated due to defects and impurities which provide low energetic pathways for drift currents. Intermediate states induced by Ag MNPs provide these pathways and increasing amounts of Ag, increases the number of low energetic routes. Furthermore, since photo-excitation is absent in dark conditions, the recombination mechanism is predominant. Thus, the higher dark currents at higher composite loadings can be rationalized, which in-turn confirms the results obtained with bode phase analysis.

To observe the hysteresis behavior of the fabricated DSCs, a forward scan (0–0.8 V) and a reverse scan (0.8–0 V) was carried out at 100 mV s⁻¹ for each DSC (Chen et al., 2016; Elbohy et al., 2019; Wu et al., 2017). Fig. 11 displays the hysteresis behavior of the DSCs with reference P25 photoanode and the optimum 1.0 mg Ag/AgBr/TiO₂ composite loaded photoanode. The hysteresis behavior in the B3 DSC *J-V* curve is slightly more pronounced than that of the B1 reference DSC. The hysteresis in DSCs is mainly caused by charge trapping and de-trapping of the semi-conductive materials due to the existence of surface/intermediate energy states (Wu et al., 2017). The Ag/AgBr/TiO₂ composite in B3 DSC carries metallic Ag particles which introduces energy states in the bandgap of TiO₂ and these states along with the surface states of TiO₂ could accumulate more charges in the forward scan mode. In the reverse scan, these accumulated electrons may contribute as capacitive current along with the photocurrent resulting in a higher J_{sc} values than the forward scan, and thus shows higher hysteresis compared to the reference cell.

3.5. Proposed mechanism of Ag/AgBr/TiO₂ as a co-sensitizer in dye-sensitized solar cells

Considering all material characteristics, parametric variations discussed under Section 3, and the energy landscape presented in Fig. 12, a

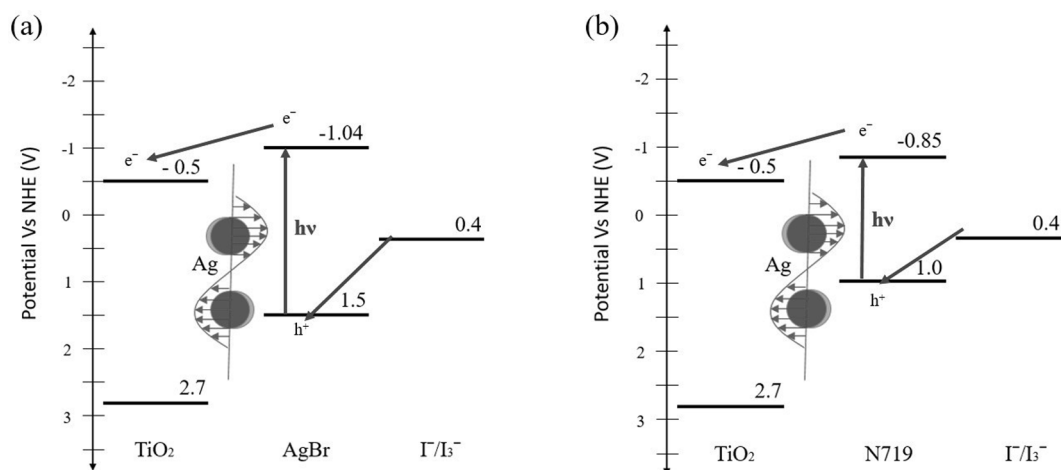


Fig. 12. Synergistic photoresponse and electron transport mechanism (a) in Ag/AgBr/TiO₂ systems, (b) with Ag in N719/TiO₂.

possible overall mechanism for Ag/AgBr/TiO₂ composite's role in a DSC can be proposed as follows. AgBr is a well-known photosensitive semiconductor material with an indirect bandgap of 2.6 eV (Glaus and Calzaferri, 2003), which is highly responsive to approximately 450–500 nm visible light. Thus, it is a possible co-sensitizer material for DSCs alongside the N719 dye. However, at illumination, the interstitial Ag⁺ cations tend to capture photogenerated electrons and form Ag clusters causing the decomposition of AgBr. This decomposition is controlled to some extent by using the support matrix TiO₂ wide bandgap semiconductor. TiO₂ having a more positive CB (−0.5 V vs NHE) than the CB of AgBr (−1.04 V vs NHE) (Hu et al., 2006; D. Wang et al., 2012; X. Wang et al., 2012), can efficiently collect the photogenerated electrons of AgBr with the aid of formed metallic Ag clusters, leaving less electron to be captured by interstitial Ag⁺. Thus, when supported on a TiO₂ matrix, even though AgBr does form Ag⁰ in early stages which is inevitable due to inherent material properties, under extended illumination, becomes much more stable (X. Wang et al., 2012). The partial decomposition of AgBr to stable Ag/AgBr compounds is termed as self-sensitization (Calzaferri et al., 2001).

Ag clusters may extract electrons from AgBr to wide bandgap semiconductor acting as electron mediators, preventing recombination of excitons or further decomposition of AgBr. They would also show LSPR effect, thus generate enhanced local EM fields, which would in-turn enhance the photo excitation in AgBr. In a DSC as dyes are also present, these near field enhancements will also accelerate photo excitation of the dye and electron injection to TiO₂ matrix due to the plasmonic effect by Ag nanoparticles. The silver particles may also scatter the light, improving the optical path length of incident photons. They are also capable of generating hot electrons and holes due to LSPR effect, where electrons migrate towards TiO₂ and, holes towards AgBr valance band as per the respective semiconductors' band alignment. On the other hand, photogenerated holes of AgBr are trapped in the AgBr valance band causing effective charge separation. All these factors contribute to improved photoelectron densities and diffusion rates in the semiconductor.

Unfortunately, these metallic Ag clusters also induce back reactions of photoelectrons with the I₃[−] ion in the redox electrolyte, alongside the forward electron transfer mechanisms discussed above. These back reactions occur due to the mid gap energy levels introduced by Ag⁰ at higher composite loadings, and have been brought to attention through EIS bode phase and dark I-V measurements. However, as is evident by the J-V, IPCE results and also EIS impedance spectra, there should be a trade-off between forward and backward electron transfer mechanisms. Thus, there should be an optimum Ag/AgBr/TiO₂ composite loading of 1.0 mg, where the generation, separation and mediation of photo-generated charges are most efficient than recombination. In addition,

the holes in the AgBr VB (1.5 V vs NHE) (Zhang et al., 2017) are at positive energy levels than the redox potential energy of the I₃[−]/I₃[−] redox couple (0.4 V vs NHE) (Li et al., 2014). Thus, proving very beneficial for DSC charge transfer mechanism, the VB holes can be effectively reduced by I[−] species, completing the current conducting pathway through the cell. Some preliminary stability tests were also conducted and it was evident that the B3 cell undergoes faster degradation than the reference B1 cell. It is quite expected, as it is known that metal halides show quick photo/thermal/chemical degradation. This will be addressed in a separate, future study focused on the stability issue.

4. Conclusion

In conclusion, a novel plasmonic and highly efficient visible light sensitive Ag/AgBr/TiO₂ composite was fabricated and was successfully incorporated in N719 dye-sensitized solar cells as a co-sensitizer. The composite carries two visible-light active components (AgBr and Ag clusters), which is the key reason for the high photocurrents and PCEs obtained for cells with composite incorporated photoanodes. Together with TiO₂ matrix as a stability enhancer, the three component composite system has proven to be an efficient active material to be used as photoanodes in dye-sensitized solar cells. Whilst, AgBr actively produces visible light excited photocharge, the Ag clusters act as perfect charge separators, mediating the photogenerated electrons on to TiO₂ semiconductor by plasmonic effect and trapping the resultant holes in AgBr itself. However, due to unfavourable recombination mechanisms introduced by Ag clusters, an optimum weight of 1.0 mg of Ag/AgBr/TiO₂ composite in the photoanode active material appears to exhibit the highest cell performance. The 1.0 mg composite containing DSC showcased the highest short circuit current density of 18.78 mA cm^{−2} while achieving a maximum power conversion efficiency of 8.46% which is 31.16% higher than that of the reference P25 DSC. This impressive efficiency enhancement is due to the synergistic effect of enhanced visible photon to current conversion, plasmonic enhancements and fast charge transfer. Thus, it could be concluded, that in addition to the well-established photocatalytic nature of the Ag/AgBr/TiO₂ composite, it could also be successfully utilized in dye-sensitized solar cells to optimize their efficiency.

Declaration of Competing Interest

The authors declare that they have no known competing financial interests or personal relationships that could have appeared to influence the work reported in this paper.

Acknowledgements

The authors gratefully acknowledge the financial support provided by the NSF under the Grant No NSF/RG/2018/BS/01 and National Institute of Fundamental Studies (NIFS), Kandy, Sri Lanka for providing research laboratory facilities.

References

- Abdellah, I.M., El-Shafei, A., 2019. The molecular engineering, synthesis and photovoltaic studies of a novel highly efficient Ru(II) complex incorporating a bulky TPA ancillary ligand for DSSCs: Donor: versus π -spacer effects. *RSC Adv.* 10, 610–619. <https://doi.org/10.1039/c9ra06150a>.
- Andualem, A., Demiss, S., 2019. Review on Dye sensitized solar cells (DSSC). *J. Heterocycl. Chem.* 1, 29–34. <https://doi.org/10.33805/2639-6734.103>.
- Ashraf, S., Su, R., Akhtar, J., Siddiqi, H.M., El-Shafei, A., 2018. Influence of brominated-TPA-stilbazole based ancillary ligand on the photocurrent and photovoltage in dye-sensitized solar cells. *Dye. Pigment.* 150, 347–353. <https://doi.org/10.1016/j.dyepig.2017.12.035>.
- Bequerel, E., 1839. Report on the electrical effects produced under the influence of solar rays.
- Bai, L., Liu, J., Tang, Y., Wang, C., Wen, J., Wu, H., He, W., Sun, R., 2020. Synergistic enhancements in the performances of dye-sensitized solar cells by the scattering and plasmon resonance of Au-nanoparticle multi-shell hollow nanospheres. *Int. J. Energy Res.* 44 (8), 7026–7034. <https://doi.org/10.1002/er.5365>.
- Bose, D.N., Govindacharyulu, P.A., 1980. Physics of silver halides and their applications. *Bull. Mater. Sci.* 2 (4), 221–231. <https://doi.org/10.1007/BF02802059>.
- Boxi, S.S., Paria, S., 2015. Visible light induced enhanced photocatalytic degradation of organic pollutants in aqueous media using Ag doped hollow TiO₂ nanospheres. *RSC Adv.* 5 (47), 37657–37668. <https://doi.org/10.1039/C5RA03421C>.
- Calzaferri, G., Brühwiler, D., Glaus, S., Schürch, D., Currao, A., Leiggner, C., 2001. Quantum-sized silver, silver chloride and silver sulfide clusters. *J. Imaging Sci. Technol.* 45 (4), 331–339. <https://calzaferri.dcb.unibe.ch/pdf/paper24.pdf>.
- Chen, B., Yang, M., Priya, S., Zhu, K., 2016. Origin of J-V Hysteresis in Perovskite Solar Cells. *J. Phys. Chem. Lett.* 7, 905–917. <https://doi.org/10.1021/acs.jpclett.6b00215>.
- Dissanayake, M.A.K.L., Kumari, J.M.K.W., Senadeera, G.K.R., Thotawatthage, C.A., 2016. Efficiency enhancement in plasmonic dye-sensitized solar cells with TiO₂ photoanodes incorporating gold and silver nanoparticles. *J. Appl. Electrochem.* 46 (1), 47–58. <https://doi.org/10.1007/s10800-015-0886-0>.
- Dong, Y.X., Wang, X.L., Jin, E.M., Jeong, S.M., Jin, B., Lee, S.H., 2019. One-step hydrothermal synthesis of Ag decorated TiO₂ nanoparticles for dye-sensitized solar cell application. *Renew. Energy* 135, 1207–1212. <https://doi.org/10.1016/j.renene.2018.12.062>.
- Du, J., Qi, J., Wang, D., Tang, Z., 2012. Facile synthesis of Au@TiO₂ core-shell hollow spheres for dye-sensitized solar cells with remarkably improved efficiency. *Energy Environ. Sci.* 5, 6914–6918. <https://doi.org/10.1039/c2ee21264a>.
- Elbohy, H., El-Mahalawy, H., El-Ghamaz A., N., Zidan, H., 2019. Hysteresis analysis in dye-sensitized solar cell based on different metal alkali cations in the electrolyte. *Electrochim. Acta* 319, 110–117. <https://doi.org/10.1016/j.electacta.2019.06.160>.
- Gan, W., Zhang, J., Niu, H., Bao, L., Hao, H., Yan, Y., Wu, K., Fu, X., 2019. Fabrication of Ag/AgBr/TiO₂ composites with enhanced solar-light photocatalytic properties. *Colloids Surfaces A Physicochem. Eng. Asp.* 583, 123968. <https://doi.org/10.1016/j.colsurfa.2019.123968>.
- Glaus, S., Calzaferri, G., 2003. The band structures of the silver halides AgF, AgCl, and AgBr: A comparative study. *Photochem. Photobiol. Sci.* 2, 398–401. <https://doi.org/10.1039/b211678b>.
- Gong, J., Sumathy, K., Qiao, Q., Zhou, Z., 2017. Review on dye-sensitized solar cells (DSSCs): Advanced techniques and research trends. *Renew. Sustain. Energy Rev.* 68, 234–246. <https://doi.org/10.1016/j.rser.2016.09.097>.
- Hamrouni, A., Azzouzi, H., Rayes, A., Palmisano, L., Ceccato, R., Parrino, F., 2020. Enhanced solar light photocatalytic activity of Ag doped TiO₂-Ag₃PO₄ composites. *Nanomaterials* 10, 1–15. <https://doi.org/10.3390/nano10040795>.
- Hong, S.M., Lee, S., Jung, H.J., Yu, Y., Shin, J.H., Kwon, K.-Y., Choi, M.Y., 2013. Simple preparation of anatase TiO₂ nanoparticles via pulsed laser ablation in liquid. *Bull. Korean Chem. Soc.* 34 (1), 279–282. <https://doi.org/10.5012/bkcs.2013.34.1.279>.
- Hou, Y., Li, X., Zhao, Q., Quan, X., Chen, G., 2011. TiO₂ nanotube/Ag-AgBr three-component nanojunction for efficient photoconversion. *J. Mater. Chem.* 21, 18067–18076. <https://doi.org/10.1039/c1jm12788h>.
- Hu, C., Lan, Y., Qu, J., Hu, X., Wang, A., 2006. Ag/AgBr/TiO₂ visible light photocatalyst for destruction of azodyes and bacteria. *J. Phys. Chem. B* 110 (9), 4066–4072. <https://doi.org/10.1021/jp0564400>.
- Hu, H., Shen, J., Cao, X., Wang, H., Lv, H., Zhang, Y., Zhu, W., Zhao, J., Cui, C., 2017. Photo-assisted deposition of Ag nanoparticles on branched TiO₂ nanorod arrays for dye-sensitized solar cells with enhanced efficiency. *J. Alloys Compd.* 694, 653–661. <https://doi.org/10.1016/j.jallcom.2016.10.057>.
- Hwang, H.-J., Joo, S.-J., Patil, S.A., Kim, H.-S., 2017. Efficiency enhancement in dye-sensitized solar cells using the shape/size-dependent plasmonic nanocomposite photoanodes incorporating silver nanoplates. *Nanoscale* 9 (23), 7960–7969. <https://doi.org/10.1039/C7NR01059A>.
- Jiang, J., Li, H., Zhang, L., 2012. New insight into daylight photocatalysis of AgBr@Ag: Synergistic effect between semiconductor photocatalysis and plasmonic photocatalysis. *Chem. - A Eur. J.* 18, 6360–6369. <https://doi.org/10.1002/chem.201102606>.
- Kakuta, N., Goto, N., Ohkita, H., Mizushima, T., 1999. Silver Bromide as a Photocatalyst for Hydrogen Generation from CH₃OH/H₂O Solution. *J. Phys. Chem. B* 103 (29), 5917–5919. <https://doi.org/10.1021/jp990287q>.
- Krishnapriya, R., Nizamudeen, C., Saini, B., Mozumder, M.S., Sharma, R.K., Mourad, A.-H.-I., 2021. MOF-derived Co²⁺-doped TiO₂ nanoparticles as photoanodes for dye-sensitized solar cells. *Sci. Rep.* 11, 1–12. <https://doi.org/10.1038/s41598-021-95844-4>.
- Kumari, J.M.K.W., Sanjeevadarshini, N., Dissanayake, M.A.K.L., Senadeera, G.K.R., Thotawatthage, C.A., 2016. The effect of TiO₂ photo anode film thickness on photovoltaic properties of dye-sensitized solar cells. *Ceylon J. Sci.* 45 (1), 33. <https://doi.org/10.4038/cjs.v45i1.7362>.
- Kumari, J.M.K.W., Senadeera, G.K.R., Dissanayake, M.A.K.L., Thotawatthage, C.A., 2017. Dependence of photovoltaic parameters on the size of cations adsorbed by TiO₂ photoanode in dye-sensitized solar cells. *Ionics (Kiel)*. 23 (10), 2895–2900. <https://doi.org/10.1007/s11581-017-1995-z>.
- Kumari, M.G.C.M., Perera, C.S., Dissanayake, B.S., Dissanayake, M.A.K.L., Senadeera, G.K.R., 2019. Highly efficient plasmonic dye-sensitized solar cells with silver nanowires and TiO₂ nano fibers incorporated multi-layered photoanode. *Electrochim. Acta* 298, 330–338. <https://doi.org/10.1016/j.electacta.2018.12.079>.
- Li, J., Chen, X.i., Ai, N., Hao, J., Chen, Q.i., Strauf, S., Shi, Y., 2011. Silver nanoparticle doped TiO₂ nanofiber dye sensitized solar cells. *Chem. Phys. Lett.* 514 (1–3), 141–145. <https://doi.org/10.1016/j.cplett.2011.08.048>.
- Li, L., Yang, Y., Fan, R., Jiang, Y., Wei, L., Shi, Y., Yu, J., Chen, S., Wang, P., Yang, B., Cao, W., 2014. A simple modification of near-infrared photon-to-electron response with fluorescence resonance energy transfer for dye-sensitized solar cells. *J. Power Sources* 264, 254–261. <https://doi.org/10.1016/j.jpowsour.2014.04.100>.
- Li, Y.-Y., Wang, J.-G., Liu, X.-R., Shen, C., Xie, K., Wei, B., 2017. Au/TiO₂ hollow spheres with synergistic effect of plasmonic enhancement and light scattering for improved dye-sensitized solar cells. *ACS Appl. Mater. Interfaces* 9 (37), 31691–31698. <https://doi.org/10.1021/acsami.7b04624>.
- Lim, S.P., Pandikumar, A., Lim, H.N., Ramaraj, R., Huang, N.M., 2015. Boosting photovoltaic performance of dye-sensitized solar cells using silver nanoparticle-decorated N, S-Co-doped-TiO₂ photoanode. *Sci. Rep.* 5, 1–14. <https://doi.org/10.1038/srep11922>.
- Mariotti, N., Bonomo, M., Fagioli, L., Barbero, N., Gerbaldi, C., Bella, F., Barolo, C., 2020. Recent advances in eco-friendly and cost-effective materials towards sustainable dye-sensitized solar cells. *Green Chem.* 22 (21), 7168–7218. <https://doi.org/10.1039/D0GC01148G>.
- Mehmood, U., Rahman, S.-u., Harrabi, K., Hussein, I.A., Reddy, B.V.S., 2014. Recent advances in dye sensitized solar cells. *Adv. Mater. Sci. Eng.* 2014, 1–12. <https://doi.org/10.1155/2014/974782>.
- Moskovits, M., 2011. Hot electrons cross boundaries. *Science* (80-) 332 (6030), 676–677. <https://doi.org/10.1126/science.1205312>.
- Musila, N., Munji, M., Simiyu, J., Masika, E., Nyenge, R., 2018. Effect of TiO₂ Compact Layer on DSSC Performance. *Path Sci.* 4 (9), 5001–5008. <https://doi.org/10.22178/pos.38-10>.
- Nazeeruddin, M.K., Kay, A., Rodicio, I., Humphry-Baker, R., Müller, E., Liska, P., Vlachopoulos, N., Grätzel, M., 1993. Conversion of Light to Electricity by cis-XzBis (2,2'-bipyridyl)-4,4'-dicarboxylate) ruthenium(II) Charge-Transfer Sensitizers (X = Cl⁻, Br⁻, I⁻, CN⁻, and SCN⁻) on Nanocrystalline TiO₂ Electrodes. *J. Am. Chem. Soc.* 115, 6382. <https://doi.org/10.1021/ja00067a063>.
- O'Regan, B., Grätzel, M., 1991. A low-cost, high-efficiency solar cell based on dye-sensitized colloidal TiO₂ films. *Nature* 353 (6346), 737–740. <https://doi.org/10.1038/353737a0>.
- Pal, A., Jana, A., Bhattacharya, S., Datta, J., 2017. SPR effect of AgNPs decorated TiO₂ in DSSC using TPMPi in the electrolyte: Approach towards low light trapping. *Electrochim. Acta* 243, 33–43. <https://doi.org/10.1016/j.electacta.2017.05.051>.
- Pastor-Moreno, G., Riley, D.J., 2002. Electrochemical studies of moderately boron doped diamond in non aqueous electrolyte. *Electrochim. Acta* 47 (16), 2589–2595. <https://doi.org/10.1016/j.electacta.2002.06.019>.
- Rawal, S.B., Bera, S., Lee, D., Jang, D.J., Lee, W.I., 2013. Design of visible-light photocatalysts by coupling of narrow bandgap semiconductors and TiO₂: Effect of their relative energy band positions on the photocatalytic efficiency. *Catal. Sci. Technol.* 3, 1822–1830. <https://doi.org/10.1039/c3cy00004d>.
- Rho, W.Y., Kim, H.S., Chung, W.J., Suh, J.S., Jun, B.H., Hahn, Y.B., 2018. Enhancement of power conversion efficiency with TiO₂ nanoparticles/nanotubes-silver nanoparticles composites in dye-sensitized solar cells. *Appl. Surf. Sci.* 429, 23–28. <https://doi.org/10.1016/j.apsusc.2017.06.258>.
- Sarker, S., Ahammad, A.J.S., Seo, H.W., Kim, D.M., 2014. Electrochemical impedance spectra of dye-sensitized solar cells: Fundamentals and spreadsheet calculation. *Int. J. Photoenergy* 2014, 1–17. <https://doi.org/10.1155/2014/851705>.
- Sharma, K., Sharma, V., Sharma, S.S., 2018. Dye-Sensitized Solar Cells: Fundamentals and Current Status. *Nanoscale Res. Lett.* 13 (1) <https://doi.org/10.1186/s11671-018-2760-6>.
- Su, R., Ashraf, S., Lyu, L., El-Shafei, A., 2020. Tailoring dual-channel anchorable organic sensitizers with indolo[2,3-b]quinoxaline moieties: Correlation between structure and DSSC performance. *Sol. Energy* 206, 443–454. <https://doi.org/10.1016/j.solener.2020.06.020>.
- Suwarnkar, M.B., Dhabbe, R.S., Kadam, A.N., Garadkar, K.M., 2014. Enhanced photocatalytic activity of Ag doped TiO₂ nanoparticles synthesized by a microwave assisted method. *Ceram. Int.* 40 (4), 5489–5496. <https://doi.org/10.1016/j.ceramint.2013.10.137>.
- Wang, D., Duan, Y., Luo, Q., Li, X., An, J., Bao, L., Shi, L., 2012a. Novel preparation method for a new visible light photocatalyst: Mesoporous TiO₂ supported Ag/AgBr. *J. Mater. Chem.* 22, 4847–4854. <https://doi.org/10.1039/C2JM14628B>.

- Wang, P., Huang, B., Dai, Y., Whangbo, M.H., 2012b. Plasmonic Photocatalysts: Harvesting Visible Light with Noble Metal Nanoparticles. *J. Mater. Chem. C* 14, 9813–9825. <https://doi.org/10.1039/C2CP40823F>.
- Wang, P., Huang, B., Zhang, X., Qin, X., Jin, H., Dai, Y., Wang, Z., Wei, J., Zhan, J., Wang, S., Wang, J., Whangbo, M.-H., 2009. Highly efficient visible-light plasmonic photocatalyst Ag@AgBr. *Chem. - A Eur. J.* 15 (8), 1821–1824. <https://doi.org/10.1002/chem.v15:810.1002/chem.200802327>.
- Wang, Q., Qiao, J., Jin, R., Xu, X., Gao, S., 2015. Fabrication of plasmonic AgBr/Ag nanoparticles-sensitized TiO₂ nanotube arrays and their enhanced photo-conversion and photoelectrocatalytic properties. *J. Power Sources* 277, 480–485. <https://doi.org/10.1016/j.jpowsour.2014.08.061>.
- Wang, X., Tang, Y., Chen, Z., Lim, T.T., 2012c. Highly stable heterostructured Ag-AgBr/TiO₂ composite: A bifunctional visible-light active photocatalyst for destruction of ibuprofen and bacteria. *J. Mater. Chem.* 22, 23149–23158. <https://doi.org/10.1039/c2jm35503e>.
- Wu, F., Li, X., Tong, Y., Zhang, T., 2017. Hysteresis analysis in dye-sensitized solar cells based on external bias field effects. *J. Power Sources* 342, 704–708. <https://doi.org/10.1016/j.jpowsour.2017.01.002>.
- Xue, C., Yan, X., Ding, S., Yang, G., 2016. Monodisperse Ag-AgBr nanocrystals anchored on one-dimensional TiO₂ nanotubes with efficient plasmon-assisted photocatalytic performance. *RSC Adv.* 6 (73), 68653–68662. <https://doi.org/10.1039/C6RA13269C>.
- Yang, L.u., Ye, F., Liu, P., Wang, F., 2016. The Visible-Light Photocatalytic Activity and Antibacterial Performance of Ag/AgBr/TiO₂ Immobilized on Activated Carbon. *Photochem. Photobiol.* 92 (6), 800–807. <https://doi.org/10.1111/php.12653>.
- Yu, J., Dai, G., Huang, B., 2009. Fabrication and characterization of visible-light-driven plasmonic photocatalyst Ag/AgCl/TiO₂ nanotube arrays. *J. Phys. Chem. C* 113 (37), 16394–16401. <https://doi.org/10.1021/jp905247j>.
- Zhang, C., Hua, H., Liu, J., Han, X., Liu, Q., Wei, Z., Shao, C., Hu, C., 2017. Enhanced photocatalytic activity of nanoparticle-aggregated ag-agx(X 5 cl, br)@tio2 microspheres under visible light. *Nano-Micro Lett.* 9, 1–13. <https://doi.org/10.1007/s40820-017-0150-8>.
- Zhang, J., Tian, B., Wang, L., Xing, M., Lei, J., 2018. Syntheses and Applications of Silver Halide-Based Photocatalysts. *Photocatalysis.* 307–343. https://doi.org/10.1007/978-981-13-2113-9_13.
- Zhang, X.G., 2005. Basic Theories of Semiconductor Electrochemistry. In: *Electrochemistry of Silicon and Its Oxide*. Springer, Boston, MA, pp. 1–43. https://doi.org/10.1007/0-306-47921-4_1.